Large uncertainties in global hydroxyl projections tied to fate of reactive nitrogen and carbon

Lee T. Murray[a,1], **Arlene M. Fiore**[b], **Drew T. Shindell**[c], **Vaishali Naik**[d], **and Larry W. Horowitz**[d]

[a]Department of Earth and Environmental Sciences, University of Rochester, Rochester, NY 14627; [b]Department of Earth and Environmental Sciences and Lamont-Doherty Earth Observatory of Columbia University, Palisades, NY 10964; [c]Nicholas School of the Environment, Duke University, Durham, NC 27708; [d]Geophysical Fluid Dynamics Laboratory, National Oceanic and Atmospheric Administration, Princeton, NJ 08540

This manuscript was compiled on August 17, 2021

The hydroxyl radical (OH) sets the oxidative capacity of the atmosphere, and thus the removal rate of pollutants and reactive greenhouse gases. While observationally derived constraints exist for global annual mean present-day OH abundances and interannual variability, OH estimates for past and future periods rely primarily on global atmospheric chemistry models. These models disagree $\pm$ 30 % in mean OH and in its changes from the pre-industrial to late 21st century, even when forced with identical anthropogenic emissions. A simple steady-state relationship that accounts for ozone photolysis frequencies, water vapor, and the ratio of reactive nitrogen to carbon emissions explains temporal variability within most models, but not inter-model differences. Here, we show that departure from the expected relationship reflects the treatment of reactive oxidized nitrogen species (NO_y) and the fraction of emitted carbon that reacts within each chemical mechanism. Our findings imply a need for observational constraints on NO_y partitioning and lifetime as well as the fate of carbon-containing reaction intermediates in order to better constrain models and reduce uncertainties in OH projections.

hydroxyl | atmospheric oxidative capacity

The hydroxyl radical (OH) is a keystone chemical species in the atmosphere, determining the removal rate of many trace gases of importance to climate, composition and human and ecosystem health (1). For example, reaction with OH in the troposphere* is the dominant sink for methane, a powerful greenhouse gas and precursor for tropospheric ozone, a major surface pollutant and greenhouse gas itself (2). Understanding what drives variability in OH is therefore critical for forecasting future changes in the self-cleansing capability of the atmosphere. The fundamental chemistry of background OH has been well known for decades (3–5). Nevertheless, global atmospheric chemistry models show large disagreement in mean OH and its transient response to specified changes in emissions (6, 7).

Fig. 1 shows global mean OH and its temporal evolution within the ensemble of simulations that participated in the Atmospheric Chemistry-Climate Model Intercomparison Project (ACCMIP) (10). The ACCMIP ensemble is a comprehensive suite of global three-dimensional atmospheric chemistry models driven by identical anthropogenic emission scenarios for the period 1850 to 2100 (8, 9). Despite applying identical anthropogenic emissions in all ACCMIP models, tropospheric mean abundances of OH range $\pm$ 30 % relative to the multi-model mean during the last decade of the historical simulation (gray-shaded interval of Fig. 1). The models also disagree as to whether OH increases or decreases across any prescribed emission scenario, except for a small window between 1980 and 2010 (when all increase).

Our best estimates of global mean abundance and interannual variability from OH rely on proxy measurements, particularly methyl chloroform (11), as the high reactivity and short lifetime of OH make direct measurement difficult and impractical for constraining spatial and temporal variability (12). On average, global atmospheric chemistry models cannot reproduce meridional gradients in CO and other long-lived reactants, implying possible errors in simulated OH spatial and seasonal distributions (6, 13). They also overestimate global mean OH with respect to observational constraints from the methane and methyl chloroform lifetimes (6, 7), and underestimate the magnitude of interannual variability in OH inferred from proxy observations (0.5 ± 0.4 % of year-to-year changes in the ACCMIP ensemble versus 2.3 ± 1.5 % derived from methyl chloroform (11)). These findings highlight gaps in our understanding of the processes that determine the oxidative capacity of the atmosphere and its variability, thereby hindering our ability to accurately predict its future evolution.

In contrast to the inter-model discrepancies in OH abundances, trends and variability, the models tend to produce consistent simulations for key tropospheric species that are intimately coupled with OH, such as tropospheric ozone (14). This implies that some—or even all—models are capturing mean abundances and spatial and temporal trends of longer-lived species at least partly for the wrong reasons.

Significance Statement

Reaction with OH is the dominant loss mechanism for many atmospheric gases of interest for air quality, climate change, and stratospheric ozone. Understanding how and why OH may change in the future is therefore paramount for predicting changes in the societal impacts associated with such changes. Future projections of models strongly disagree in how OH responds to changing emissions and climate – even in the sign of the change. Here, we demonstrate inter-model differences in OH are best explained by disparate implementations of chemical and physical processes that affect reactive oxides of nitrogen and organic chemical species. Targeted observations can reduce uncertainty in the chemical budgets of these key species to increase confidence in future projections of composition and its impacts.

L.T.M. designed the research; L.T.M. performed the research; A.M.F. and D.T.S. advised the research; L.T.M. wrote the paper; All authors contributed to the discussion.

The authors declare no conflict of interest.

*The lowermost several kilometers of the atmosphere in contact with the Earth's surface.

[1]To whom correspondence should be addressed. E-mail: lee.murray@rochester.edu

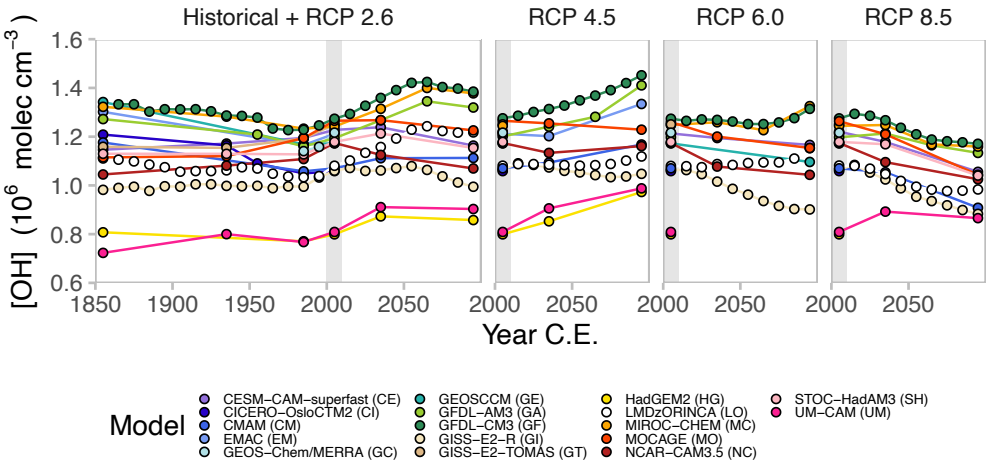

Fig. 1. Large disagreement in decadal mean tropospheric OH and its transient evolution in global atmospheric chemistry models. The models shown prescribe identical anthropogenic emissions from a historical reconstruction (8) and four possible future "Representative Concentration Pathway" (RCP) scenarios (9). Different colors represent different models. Gray rectangle highlights the period 2000-2010 in each scenario. Full model names shown in legend with a two-letter abbreviation shown in parentheses used in subsequent figures.

The original analysis of OH in the ACCMIP simulations noted that the change in OH over time in a given model correlated with the ratio of change in its burden of reactive nitrogen oxides ($NO_x \equiv NO + NO_2$) to change in its carbon monoxide (CO) burden, but did not provide a mechanistic explanation (6). Here, we re-examine the ACCMIP model ensemble through the lens of fundamental OH chemistry to explain the disparate behavior between the models. The key areas of uncertainty we identify provide a target for future observing strategies to advance most rapidly our understanding as formalized in the models used to project future atmospheric abundances of pollutants and reactive greenhouse gases.

A Steady-State Relationship for OH

The key reactions controlling OH are highly and nonlinearly coupled to one another (3–5, and see *SI* Fig. S1). In the GEOS-Chem chemistry-transport model (CTM; see Materials and Methods section), primary production of OH by photolysis or photolysis-initiated chains contributes to approximately 60 % of total production in the present day, with most of that source resulting from photolysis of ozone in the presence of water vapor. The remaining 40 % results from chemical recycling of the HO_x family ($HO_x \equiv$ OH + peroxy radicals) via reaction of peroxy radicals with reactive oxides of nitrogen (NO_x) or ozone. Loss of OH is primarily via reaction with reduced carbon species such as CO (40 %) and methane (15 %), with products of methane oxidation, other non-methane volatile organic compounds (NMVOCs) and their oxidation products, ozone, H_2, HO_x species, and other minor species accounting for the remainder. Here, we refer to the sum of CO, methane and all NMVOCs as total "reactive carbon."

The equations that describe the dominant OH photochemistry are simple enough that they yield an analytic solution for OH when one assumes "steady state," in which the sum of the source terms is balanced by all loss terms (see *SI* Sect. S1). At steady state, variations in OH should vary proportional to

$$J_{O(^1D)}\ q\ \frac{S_N}{S_C^{3/2}}, \qquad [1]$$

where $J_{O(^1D)}$ is the photolysis frequency of ozone to $O(^1D)$ (s^{-1}), q is the specific humidity (kg H_2O kg air^{-1}), and S_N and S_C are the emission rates of NO_x (Tmol N yr^{-1}) and reactive carbon (Tmol C yr^{-1}) species, respectively. The first two terms limit the rate of total HO_x production whereas the emission ratio determines the relative partitioning of HO_x between OH and peroxy radicals (with nitrogen oxides favoring OH and reactive carbon favoring peroxy radicals). The exponent in the denominator accounts for nonlinear feedbacks in the coupled chemistry. Collectively, the relationship describes how the basic OH photochemistry changes in response to changing emissions and climate parameters. Eq. [1] has been previously used to explain global OH variability within a single CTM across a wide range of climate and emissions scenarios with high skill (15). However, in principal it should hold across multiple models, as it derives from the analytic solution to the steady-state OH photochemistry.

Large temporal and inter-model variability exists within the decadal mean evolution of each component of Eq. [1] of the ACCMIP ensemble (Fig. S2). The models employed a variety of methods for determining photolysis rates, ranging from look-up tables to online calculation with column radiation codes (10). Most models agree in their mean photolysis frequencies, although outliers exist in the ensemble. Changes in photolysis frequencies with time are relatively small compared to inter-model variability, although it has been previously shown that OH is especially sensitive to them (e.g., 15–17). These temporal changes are driven primarily by changes in overhead ozone abundances associated with anthropogenic emissions of stratospheric ozone-depleting substances and greenhouse gases (18), with peak photolysis rates in each model occurring during the height of stratospheric ozone loss ca. 1980-2010. The models are in tight agreement in both tropospheric mean water vapor abundance and its exponential increase over time in response to temperature-driven increases in saturation water vapor pressure (19). NO_x emissions are dominated by the prescribed anthropogenic sources and therefore temporal variability dominates over inter-model variability. However, slight differences do exist between models and in time due to different parameterizations of climate-sensitive natural sources such as lightning (20). In contrast, emissions of reactive carbon species vary widely across the models and in time. These variations are dominated by natural sources; the models employed a wide range of biogenic NMVOC implementations with respect to species emitted (including none),

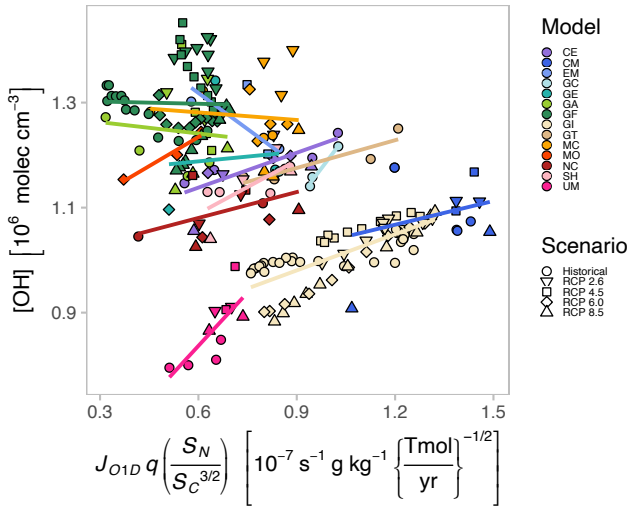

Fig. 2. Decadal mean OH as a function of the steady-state photochemical relationship. Variability within many individual models is accurately explained by Eq. [1]. However, large inter-model variability is not. Individual models are identified by color and emission scenario by shape. An ordinary linear regression line is shown for each model sub-population. See *SI* Fig. S3 for individual model detail at annual time scales.

chemical mechanism, base emissions, and the response of emissions to changes in meteorology, e.g., the increase in isoprene emission by terrestrial plants at warmer temperatures (21).

Fig. 2 shows decadal mean OH in the ACCMIP simulations as a function of Eq. [1]. If differences in the four key parameters in Fig. S2 were sufficient to explain OH variability within and between the models then all points would fall on the same line with a positive slope. The OH steady-state predictor is usually sufficient to explain variability within individual models, although not in the models with the highest mean OH abundances. A large mode of residual inter-model variability dominates the ensemble variability. This inter-model variability lies largely orthogonal to that explained by the OH photochemistry, and is therefore likely independent.

Fig. 3 shows that the residual variability can be best explained by considering two new parameters derived from available ACCMIP model diagnostics. First, the large inter-model variability is primarily related to the NMVOC "oxidation efficiency," ϵ_C, which we define as the fraction of carbon atoms emitted in NMVOC compounds oxidized to CO before removal from the atmosphere (units of mol C per mol C). Models that have a higher fraction of their emitted carbon converted to CO tend to have lower OH (Fig. 3a). Second, departure from linearity within a single model is primarily related to shifts in the tropospheric lifetime of NO_x, τ_{NO_x} (units of time; Fig. 3b). Variations in these two parameters act to alter the magnitude of the HO_x partitioning response to changes in emissions of NO_x versus reduced carbon species in Eq. [1].

Factors Driving Model Diversity

The most apparent correlation of inter-model variability in Fig. 3 is with the NMVOC oxidative efficiency (ϵ_C), with models having higher ϵ_C tending to have lower OH. While the greatest sinks of OH are CO and methane, respectively, these do not vary much between the ACCMIP models by design; methane and anthropogenic CO are prescribed, and nearly all methane is oxidized to CO (22). The large inter-model variability in NMVOC emissions are not correlated with inter-model variability in global mean OH, even though NMVOCs consume OH, because relatively short NMVOC lifetimes restrict their influence to be immediately downwind of sources, which are mostly in the continental boundary layer. Instead, differences in the portion of NMVOCs fully oxidized to CO (i.e. ϵ_C), a gas with a sufficiently long lifetime to mix into the free and remote troposphere, best explain inter-model variability in global mean OH.

From the perspective of reactive carbon, the atmosphere is a low-temperature furnace: reduced organic gases are emitted and subsequently oxidized through a chain of increasingly semi-oxidized species toward CO and CO_2. However, increased oxidation tends toward lower-volatility species that may condense (23). Other intermediates are soluble and/or prone to surface uptake, and physical processes may siphon these from the atmosphere as well. All in all, physical loss is a greater atmospheric sink of NMVOC carbon than chemical conversion to CO and CO_2 in most models (ϵ_C often <0.5; Figs. 3a and S4; also 24–26).

Atmospheric model developers must make choices that influence an individual model's oxidative efficiency. We must balance a yet imperfect scientific understanding of atmospheric oxidation mechanisms (e.g., 27) with desired model capabilities and computational limitations. Near-explicit mechanisms using elementary reactions based on observational constraints for the oxidation of isoprene alone would require thousands of reactions and several hundred species (28), intractable for global atmospheric models. For these reasons, global models typically employ reduced chemical mechanisms with lumped surrogate species and empirically-derived stoichiometries in order to best reproduce observations within computational limits.

We highlight two end members of the ACCMIP ensemble by contrasting the hydrocarbon oxidation mechanisms of the Goddard Institute for Space Studies (GISS) and Geophysical Fluid Dynamics Laboratory (GFDL) models. In the GISS model (Fig. S5), gaseous NMVOCs are emitted as 2 explicit and 3 lumped species, transforming among 18 NMVOC species before conversion to CO. All oxidation pathways lead to CO, except for seven species (39 %) that may be physically removed, and a terminal pathway included to enable tuning of relative oxidation rates to observations (29). In contrast, the GFDL model (Fig. S6) emits NMVOCs as 10 explicit and 2 lumped species, transforms among 44 total NMVOC species, with 28 species (64 %) physically removable by wet or dry processes. Furthermore, the GFDL empirical oxidation stochiometries include partial direct conversion of NMVOCs to CO_2, bypassing CO. Given the greater opportunity for loss of intermediates, only 23 % of NMVOC emitted by the GFDL model is oxidized to CO, versus 53 % in the GISS model. Consequently, the GISS model has a greater fraction of its emitted reactive carbon reacting with OH, and thereby lower OH.

Despite large inter-model variability, the oxidative efficiency is relatively invariant in time for a given model (Fig. S7). This implies that the oxidative efficiency is primarily determined by the specific combination of species, reactions and sinks implemented in a given model. Nevertheless, minor temporal changes occur, reflecting shifts in the distribution and magnitudes of reactive carbon emissions and pre-

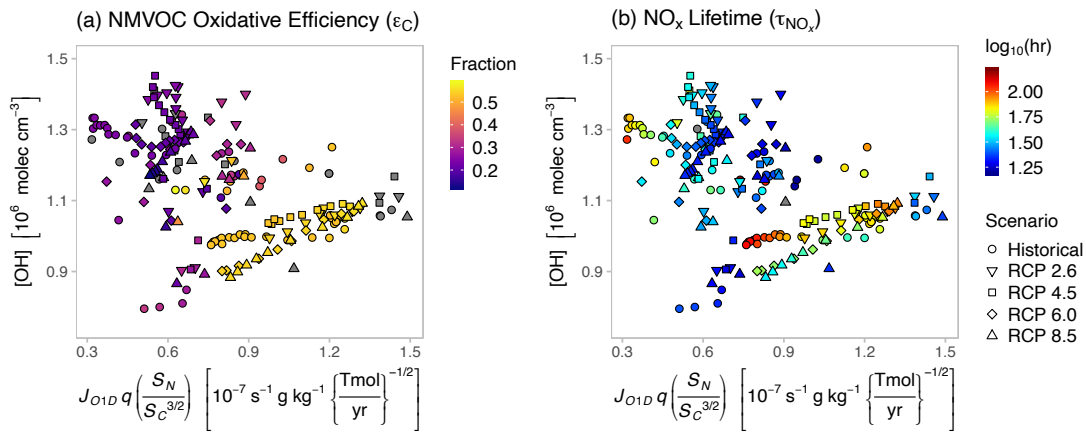

Fig. 3. Residual inter- and intra-model variability of Fig. 2 explained by two parameters. Panel (a) shows the points of Fig. 2 colored by their decadal mean "oxidative efficiency," the fraction of emitted NMVOC carbon that is oxidized to CO before atmospheric removal. Panel (b) shows the points colored by τ_{NO_x}, i.e. the NO_x burden ($\equiv NO + NO_2$) divided by its source. Gray-shaded points indicate insufficient model data archived for calculation.

cipitation. For example, the methane increase in the RCP 8.5 scenario consumes a larger fraction of OH, slowing the oxidation rate of NMVOCs, allowing more time for intermediate species to be lost via deposition, thereby reducing ϵ_C in some models.

In contrast to ϵ_C, variability in τ_{NO_x} contributes to both inter- and intra-model variability in OH. The rapid cycling of NO_x between NO and NO_2 allows for the catalytic production of relatively large quantities of OH (Fig. S8), otherwise all OH would be quickly titrated from the atmosphere. Longer τ_{NO_x} enables relatively more OH production per NO_x molecule. Global mean τ_{NO_x} varies by orders of magnitude across models (Fig. 3b) and some models simulate temporal changes by nearly as much, although others suggest little change (Fig. S7). Therefore, variations in τ_{NO_x} can influence both inter- and intra-model changes in global mean OH. Fig. S9 demonstrates the sensitivity of the steady-state OH abundance to mean τ_{NO_x} in the GFDL model. The factors controlling the lifetime of NO_x are many and can compete in sign. We next demonstrate the sensitivity of global mean OH to three key parameters with known inter-model disparities.

First, the ACCMIP models employ very different vertical and meridional distributions of lightning NO_x (cf. Fig. 3 of ref. 20). Because τ_{NO_x} increases exponentially with altitude, global mean τ_{NO_x} is highly sensitive to the mean vertical injection height of lightning NO_x. Most models release lightning NO_x into the free troposphere. However, two ACCMIP ensemble members (UM and HG) release their lightning NO_x primarily into the boundary layer. When we compare a sensitivity simulation using the GEOS-Chem CTM with lightning NO_x released at the surface instead of at altitude, global mean OH decreases by 22% (Fig. 4a), a sizable portion of the difference in OH between GEOS-Chem and the two ACCMIP models releasing all lightning NO_x near the surface (Fig. 4d).

Second, heterogeneous reactions can vary substantially between global models. Uptake of gaseous species on the surface of aerosol particles is a highly efficient means for sequestering NO_y and HO_x from the atmosphere, short-circuiting the OH photochemistry included in Eq. 1. Most models include hydrolysis of N_2O_5 on aerosol particles, often the dominant local sink for NO_y, with a known strong influence on global OH (30, 31). However, models differ in implementation (e.g., some models vary the uptake coefficient γ with aerosol composition) as well as in the inclusion of other heterogeneous losses. When we disable heterogeneous losses within GEOS-Chem (normally N_2O_5 hydrolysis with $\gamma_{N_2O_5} \leq 0.02$ (32) and HO_2 uptake with $\gamma_{HO_2} \leq 0.1$ (33)), global mean OH increases by 12 % (Fig. 4b), the magnitude of many inter-model differences. We note that the only difference in the gas-phase chemistry of the two variants of the GISS model submitted

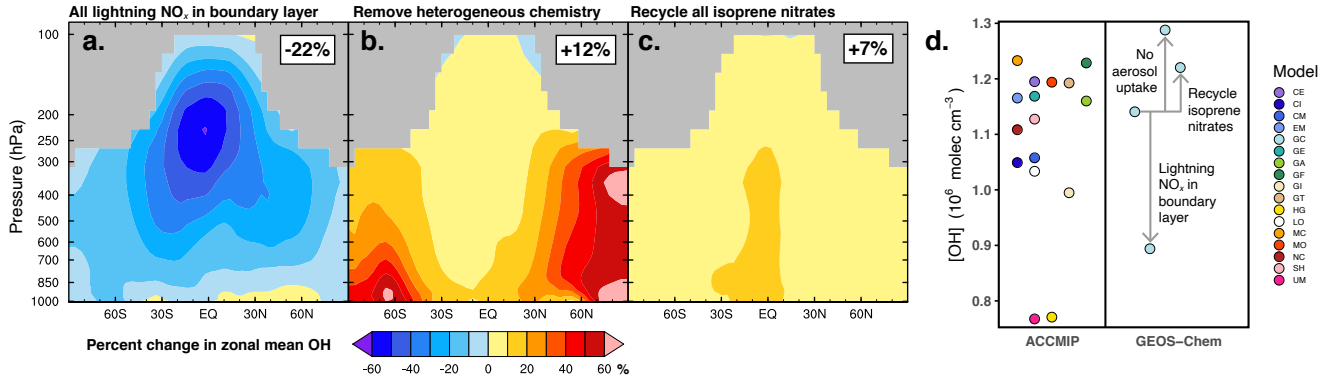

Fig. 4. Global mean OH is highly sensitive to the treatment of reactive nitrogen. Change in zonal mean OH in the GEOS-Chem CTM for the year 1980 for the following scenarios: (a) all lightning NO_x is released into the planetary boundary layer instead of at altitude, (b) all heterogeneous reactions are turned off, and (c) all nitrogen sequestered in isoprene nitrates is recycled back to NO_x. The box reports the percent change in the global OH burden. Panel (d) shows decadal mean OH in the ACCMIP models for the 1980s vs. that in GEOS-Chem and the three sensitivity simulations shown in panels (a)-(c). The x-axis is arbitrary.

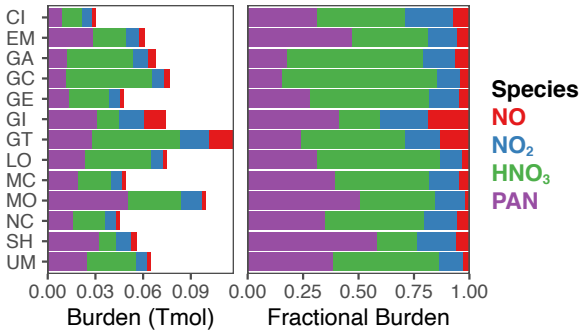

Fig. 5. ACCMIP models show large disagreement in their reactive nitrogen budgets. Left panel shows the cumulative absolute burdens of the four dominant NO_y species: peroxyacetylnitrate (PAN), HNO_3, NO_2, and NO. Decadal tropospheric mean shown for the 2000s from 13 global atmospheric chemistry models. The right panel shows the cumulative fractional burdens per model.

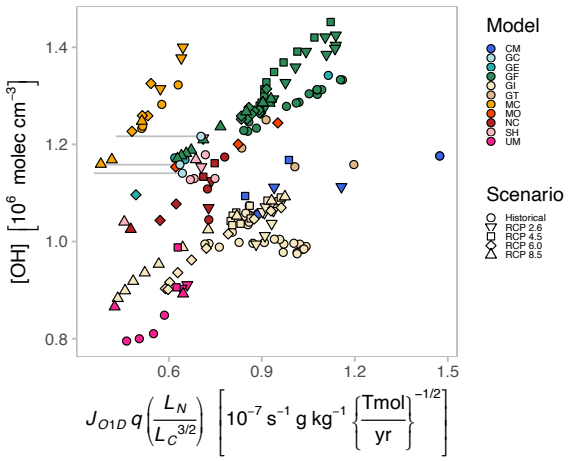

Fig. 6. Variability in decadal mean OH in the ACCMIP simulations is better captured when considering photochemical sinks of reactive nitrogen and carbon (as in this figure) than sources (as in Fig. 2). Instead of emission, we apply the total loss rate of CO and methane (L_C), which is equivalent to the sum of the sources of CO, methane and the oxidative efficiency times the NMVOC source. Furthermore, we estimate the loss of NO_x to nitric acid (L_N). See Methods and Materials for details. Gray horizontal lines indicate the error in estimating L_N from archived monthly-mean values relative to online calculation with GEOS-Chem (not archived by the ACCMIP experiment).

to the ACCMIP study was that one included heterogeneous uptake of HNO_3 on dust particles (GI; 34) and one did not (GT), resulting in a longer τ_{NO_x} and 20 % higher OH in the latter (Fig. 4d).

Lastly, NO_y is often stored in relatively long-lived reservoir species, which prolong and redistribute the influence of NO_x on oxidants. However, these reservoir species may also be lost to deposition, which bypasses the assumption that all NO_x is lost via oxidation to HNO_3 intrinsic to Eq. 1. One particular area of model diversity in NO_y reservoirs regards the fate of isoprene nitrates, products of oxidation of isoprene by NO_x, especially at night. Some chemical mechanisms, including that implemented in our version of GEOS-Chem, assume that this nitrate is immediately lost to deposition, reflecting observational evidence that this can be a major local NO_y sink (e.g., 35). Others allow for part of this nitrate to be recycled back to NO_x. When we perform a sensitivity test in GEOS-Chem in which we allow all isoprene nitrates to be recycled back to NO_x, global mean OH increases by 7 % (Fig. 4c), the magnitude of differences between GEOS-Chem and the GFDL model (GA, GF), which included isoprene nitrate recycling (albeit, <100 %; 36).

Disparate implementations of processes that affect τ_{NO_x} therefore cause the NO_y budget to be a key source of model uncertainty with respect to OH. Fig. 5 shows that despite nearly identical NO_x emission magnitudes, the models show large variability in their absolute burdens and relative partitioning of the dominant NO_y species. This is much greater than seen in the longer-lived species such as ozone and CO. Furthermore, Fig. 5 is missing other major NO_y species not archived for ACCMIP, e.g., HONO or HO_2NO_2, which likely also vary between models.

Taken together, the sensitivity of global mean OH to ϵ_C and τ_{NO_x} implies that a key assumption of Eq. 1 does not hold between models or within some models, i.e. the sources of reactive nitrogen and carbon are not balanced by their dominant sinks with respect to OH (oxidation to nitric acid and carbon dioxide, respectively). Various processes siphon emitted reactive nitrogen and carbon from the atmosphere before they may influence OH photochemistry. It is variations in the fraction of total nitrogen and carbon loss pathways that involve OH that ultimately control OH abundance in the models, and therefore the atmospheric chemistry and physics that occurs between emission and loss. Fig. 6 shows that we are better able to capture inter- and intra-model variability in OH by shifting our focus from the sources of nitrogen and carbon to the sinks ($R = 0.5$ for $n = 221$ decadal time slices).

Conclusions

Atmospheric chemistry model contributions to the ACCMIP experiment strongly disagree in their global mean OH and its transient evolution in response to prescribed changes in anthropogenic emissions (Fig. 1). A steady-state relationship derived from the basic coupled photochemistry of the O_x-HO_x-NO_x-CO system explains OH variability within models if the NO_x lifetime (τ_{NO_x}) remains relatively constant (Fig. 2). However, model OH is sensitive to inter-model differences in the fraction of non-methane volatile organic carbon that is completely oxidized through CO (and CO_2), ϵ_C, as well as τ_{NO_x} (Fig. 3). The oxidative efficiency is generally fixed for a given model, determined by the kinetics of the reactions and species included in the model. In contrast, the NO_x lifetime is much more variable between models and even within some models, and is especially sensitive to the altitude of lightning emissions, heterogeneous chemistry, and treatment of reactive nitrogen reservoir species (Fig. 4), although this list is not exhaustive. Variations in global mean OH between and within global models are therefore better characterized by variations in the relative loss pathways of reactive nitrogen and carbon than in their emissions (Fig. 6).

We recommend future efforts diagnose comprehensive reactive nitrogen budgets in models and evaluate with observations, especially in the tropical free troposphere. Likewise, we recommend future observational campaigns target quantification of the global source of CO from NMVOC oxidation. Improved observational estimates of τ_{NO_x} and ϵ_C will help to constrain models and improve projections of the future oxidizing power of the atmosphere.

Materials and Methods

A. Data analyzed. The Atmospheric Chemistry and Climate Model Intercomparison Project (ACCMIP) consisted of 16 atmospheric chemistry models driven by identical anthropogenic emissions and climate forcers over the 1850-2100 period (10). Most models were run as decadal time-slice experiments for a few core decades (1850s, 1980s, 2000s, 2030s, 2090s), although the GISS-E2-R model submitted its transient simulations for the Coupled Model Intercomparison Project Phase 5 (CMIP5). The ACCMIP and CMIP5 simulations were performed in support of the Fifth Assessment Report of the Intergovernmental Panel on Climate Change. The diagnostics saved for the ACCMIP study are archived at the British Atmospheric Data Centre (http://badc.nerc.ac.uk), as downloaded in Sept. 2019. Here we analyze the historical simulations and the four future RCP scenarios (9). All 3-d and 2-d variables were processed at monthly temporal resolution by integrating tropospheric totals or airmass-weighted mean values, as appropriate. The troposphere is defined with a monthly chemical tropopause of 150 ppbv ozone, consistent with earlier ACCMIP analyses (6, 7, 14). The monthly values are then averaged to obtain decadal means. We supplement the ACCMIP data with transient runs from the GFDL-CM3 contribution to the CMIP5 study that used the same emissions and forcings (37) and GEOS-Chem (next subsection).

Ozone photolysis is directly archived (*photo1d*) or estimated from the archived OH production rate (*prodohjo3*) using coefficients from the JPL Handbook (38). Specific humidity is archived as *hus*. S_N is archived as *eminox*. S_C is the sum of total emission of CO (*emico*), NMVOCs (*emivoc*) and methane, which we assume is equivalent to the total loss rate of methane (*lossch4*). Emission totals are adjusted to match values self-reported by the modeling groups in Lamarque et al. (10), as outlined in the *SI* Sect. S2. By assuming that direct emissions and chemical production of CO from methane and NMVOCs are balanced by its total chemical loss, then the oxidative efficiency can be estimated as $\epsilon_C \equiv \frac{P(\mathrm{CO})_{\mathrm{NMVOC}}}{E_{\mathrm{NMVOC}}} \approx \frac{L(\mathrm{CO}) - E_{\mathrm{CO}} - P(\mathrm{CO})_{\mathrm{CH_4}}}{E_{\mathrm{NMVOC}}}$. Total chemical loss of CO was archived as *lossco*, and again we use *emivoc* and *emico*. We estimate the source of CO from methane oxidation by assuming a 100 % conversion of oxidized methane from *lossch4* to CO (22). τ_{NO_x} is determined as the total burden of NO (*vmrno*) and NO_2 (*vmrno2*) divided by the total source (*eminox*).

To adjust the steady-state relationship for Fig. 6, we estimate L_C as *lossco* + *lossch4*, which neglects carbon lost to intermediates. We estimate L_N as the production rate of HNO_3 from the pressure-dependent NO_2 + OH reaction using monthly archived NO_2, OH, air density, and temperature, and rate constants from ref. (38).

B. Original simulation description. We use the default GEOS-Chem global CTM (v9-01-03; available at http://www.geos-chem.org) with its "tropchem" mechanism driven by MERRA reanalysis meteorological fields (39) degraded to 4° latitude by 5° longitude by 47 vertical levels (38 in the troposphere), and the same emissions used in the ACCMIP study. Methane is prescribed as a surface boundary condition and allowed to advect and react, consistent with the ACCMIP models. The base simulation is initialized over the year 1979, and then archived for 1980-2010. NO_x sensitivity experiments are then performed by re-initializing over 1979 and archiving year 1980 for the 3 scenarios described in the main text.

ACKNOWLEDGMENTS. L.T.M. was supported in part by a NASA Postdoctoral Program fellowship administered by the Universities Space Research Association. A.M.F. acknowledges support from NASA ACMAP (NNX17AG40G). D.T.S. acknowledges support from NASA GISS (80NSSC19M0138) and the NCCS.

1. Ehhalt DH (1999) Photooxidation of trace gases in the troposphere. *Phys Chem Chem Phys* 1(24):5401–5408.
2. IPCC (2013) *Climate Change 2013: The Physical Science Basis*, Contribution of Working Group I to the Fifth Assessment Report of the Intergovernmental Panel on Climate Change eds. Stocker TF, et al. (Cambridge University Press, Cambridge, UK and New York, NY, USA).
3. Levy II H (1971) Normal Atmosphere: Large Radical and Formaldehyde Concentrations Predicted. *Science* 173(3992):141–143.
4. Logan JA, Prather MJ, Wofsy SC, McElroy MB (1981) Tropospheric chemistry: A global perspective. *J Geophys Res* 86(C8):7210–7254.
5. Spivakovsky CM, et al. (2000) Three-dimensional climatological distribution of tropospheric OH: Update and evaluation. *J Geophys Res* 105(D7):8931.
6. Naik V, et al. (2013) Preindustrial to present-day changes in tropospheric hydroxyl radical and methane lifetime from the Atmospheric Chemistry and Climate Model Intercomparison Project (ACCMIP). *Atmos Chem Phys* 13(10):5277–5298.
7. Voulgarakis A, et al. (2013) Analysis of present day and future OH and methane lifetime in the ACCMIP simulations. *Atmos Chem Phys* 13(5):2563–2587.
8. Lamarque JF, et al. (2010) Historical (1850–2000) gridded anthropogenic and biomass burning emissions of reactive gases and aerosols: methodology and application. *Atmos Chem Phys* 10(15):7017–7039.
9. van Vuuren DP, et al. (2011) The representative concentration pathways: an overview. *Climatic Change* 109(1-2):5–31.
10. Lamarque JF, et al. (2013) The Atmospheric Chemistry and Climate Model Intercomparison Project (ACCMIP): overview and description of models, simulations and climate diagnostics. *Geosci Model Dev* 6(1):179–206.
11. Montzka SA, et al. (2011) Small Interannual Variability of Global Atmospheric Hydroxyl. *Science* 331(6013):67–69.
12. Stone D, Whalley LK, Heard DE (2012) Tropospheric OH and HO_2 radicals: field measurements and model comparisons. *Chem Soc Rev* 41(19):6348–6404.
13. Shindell DT, et al. (2006) Multimodel simulations of carbon monoxide: Comparison with observations and projected near-future changes. *J Geophys Res Atmos* 111(D19).
14. Young PJ, et al. (2013) Pre-industrial to end 21^{st} century projections of tropospheric ozone from the Atmospheric Chemistry and Climate Model Intercomparison Project (ACCMIP). *Atmos Chem Phys* 13(4):2063–2090.
15. Murray LT, et al. (2014) Factors controlling variability in the oxidative capacity of the troposphere since the Last Glacial Maximum. *Atmos Chem Phys* 14(7):3589–3622.
16. Holmes CD, Prather MJ, Søvde OA, Myhre G (2013) Future methane, hydroxyl, and their uncertainties: key climate and emission parameters for future predictions. *Atmos Chem Phys* 13(1):285–302.
17. Murray LT, Logan JA, Jacob DJ (2013) Interannual variability in tropical tropospheric ozone and OH: The role of lightning. *J Geophys Res Atmos* 118(19):11468–11480.
18. Iglesias-Suarez F, Young PJ, Wild O (2016) Stratospheric ozone change and related climate impacts over 1850–2100 as modelled by the ACCMIP ensemble. *Atmos Chem Phys* 16(1):343–363.
19. Santer BD, et al. (2007) Identification of human-induced changes in atmospheric moisture content. *P Natl Acad Sci USA* 104(39):15248–15253.
20. Murray LT (2016) Lightning NO_x and Impacts on Air Quality. *Curr Pollution Rep* 2(2):115–133.
21. Sanadze GA (2004) Biogenic Isoprene (A Review). *Russian Journal of Plant Physiology* 51(6):729–741.
22. Duncan BN, et al. (2007) Global budget of CO, 1988–1997: Source estimates and validation with a global model. *J Geophys Res* 112(D22):D22301.
23. Donahue NM, Robinson AL, Trump ER, Riipinen I, Kroll JH (2012) Volatility and Aging of Atmospheric Organic Aerosol in *Atmospheric and Aerosol Chemistry*. (Springer Berlin Heidelberg, Berlin, Heidelberg), pp. 97–143.
24. Kanakidou M, et al. (2012) Atmospheric fluxes of organic N and P to the global ocean. *Global Biogeochem Cy* 26(3):4478.
25. Edwards PM, Evans MJ (2017) A new diagnostic for tropospheric ozone production. *Atmos Chem Phys* 17(22):13669–13680.
26. Safieddine SA, Heald CL, Henderson BH (2017) The global nonmethane reactive organic carbon budget: A modeling perspective. *Geophys Res Lett* 44(8):3897–3906.
27. Wennberg PO, et al. (2018) Gas-Phase Reactions of Isoprene and its Major Oxidation Products. *Chem Rev* 118(7):3337–3390.
28. Jenkin ME, Young JC, Rickard AR (2015) The MCM v3.3.1 degradation scheme for isoprene. *Atmos Chem Phys* 15(20):11433–11459.
29. Shindell DT, Faluvegi G, Bell N (2003) Preindustrial-to-present-day radiative forcing by tropospheric ozone from improved simulations with the GISS chemistry-climate GCM. *Atmos Chem Phys* 3(5):1675–1702.
30. Dentener FJ, Crutzen PJ (1993) Reaction of N_2O_5 on Tropospheric Aerosols - Impact on the Global Distributions of NO_x, O_3, and OH. *J Geophys Res* 98(D4):7149–7163.
31. Evans MJ, Jacob DJ (2005) Impact of new laboratory studies of N_2O_5 hydrolysis on global model budgets of tropospheric nitrogen oxides, ozone, and OH. *Geophys Res Lett* 32(9):L09813.
32. Macintyre HL, Evans MJ (2010) Sensitivity of a global model to the uptake of N_2O_5 by tropospheric aerosol. *Atmos Chem Phys* 10(15):7409–7414.
33. Macintyre HL, Evans MJ (2011) Parameterisation and impact of aerosol uptake of HO_2 on a global tropospheric model. *Atmos Chem Phys* 11(21):10965–10974.
34. Bauer SE, Koch DM (2005) Impact of heterogeneous sulfate formation at mineral dust surfaces on aerosol loads and radiative forcing in the Goddard Institute for Space Studies general circulation model. *J Geophys Res* 110(D17):25251.
35. Romer PS, et al. (2016) The lifetime of nitrogen oxides in an isoprene-dominated forest. *Atmospheric Chemistry and Physics* 16(12):7623–7637.
36. Horowitz LW, et al. (2007) Observational constraints on the chemistry of isoprene nitrates over the eastern United States. *J Geophys Res* 112(D12):955.
37. John JG, Naik V, Horowitz LW, Dunne JP (2012) Climate versus emission drivers of methane lifetime against loss by tropospheric OH from 1860–2100. *Atmos Chem Phys* 12(24):12021–12036.
38. Sander SP, et al. (2011) *Chemical Kinetics and Photochemical Data for Use in Atmospheric Studies*. (JPL Publication 10-6).
39. Rienecker MM, et al. (2011) MERRA: NASA's Modern-Era Retrospective Analysis for Research and Applications. *J Climate* 24(14):3624–3648.

PNAS
www.pnas.org

Supplementary Information for

Uncertainties in global hydroxyl projections tied to fate of reactive nitrogen and carbon

Lee T. Murray, Arlene M. Fiore, Drew T. Shindell, Vaishali Naik, Larry W. Horowitz

Lee T. Murray.
E-mail: lee.murray@rochester.edu

This PDF file includes:

Supplementary text
Figs. S1 to S9
References for SI reference citations

Supporting Information Text

S1. Derivation of the steady-state relationship

Here, we derive a solution of the steady-state system of fundamental OH chemistry to relate changes in simulated global mean OH to a simple function of four convolved key parameters: ozone photolysis rates, water vapor abundances, and emissions of reactive nitrogen and carbon species. This relationship was previously applied by Murray et al. (1), and is an expansion of an earlier derivation by Wang and Jacob (2). Figure S1 shows the coupling between the dominant reactions and species that influence OH abundances.

The primary source of HO_x ($\equiv$ OH + peroxy) radicals to the troposphere is the photolysis of ozone to $O(^1D)$, followed by reaction with water vapor,

$$O_3 + h\nu \rightarrow O(^1D) + O_2 \quad [R1]$$

$$O(^1D) + H_2O \rightarrow 2OH, \quad [R2]$$

otherwise, $O(^1D)$ is quenched and reforms ozone,

$$O(^1D) + M \xrightarrow{O_2} O_3 + M \quad [R3]$$

Cycling of HO_x species during oxidation of CO in the presence of NO_x ($\equiv$ NO + NO_2) leads to ozone production,

$$CO + OH \xrightarrow{O_2} CO_2 + HO_2 \quad [R4]$$

$$HO_2 + NO \rightarrow OH + NO_2 \quad [R5]$$

$$NO_2 + h\nu \xrightarrow{O_2} NO + O_3 \quad [R6]$$

In addition to R5, the oxidation of NO to NO_2 also takes place by reaction with ozone,

$$NO + O_3 \rightarrow NO_2 + O_2 \quad [R7]$$

Loss of HO_x radicals is primarily by self-reaction of HO_2 and by oxidation of NO_2 by OH to nitric acid,

$$HO_2 + HO_2 \rightarrow H_2O_2 + O_2 \quad [R8]$$

$$NO_2 + OH \xrightarrow{M} HNO_3 \quad [R9]$$

Ozone is also transported from the stratosphere and can be lost by deposition to the surface.

The steady state equations of the system described by reactions R1 through R9 for HO_x, OH, O_3, NO_x, and CO concentrations are, respectively,

$$2\frac{J_{R1}k_{R2}[H_2O]}{k_{R3}[M]}[O_3] = 2k_{R8}[HO_2]^2 + k_{R9}[OH][NO_2][M] \quad [1]$$

$$k_{R5}[HO_2][NO] + 2\frac{J_{R1}k_{R2}[H_2O]}{k_{R3}[M]}[O_3] = k_{R4}[OH][CO] + k_{R9}[OH][NO_2][M] \quad [2]$$

$$k_{R5}[HO_2][NO] + F_{STE} = \frac{J_{R1}k_{R2}[H_2O]}{k_{R3}[M]}[O_3] + k_d[O_3] \quad [3]$$

$$S_N = L_N = k_{R9}[OH][NO_2][M] \quad [4]$$

$$S_C = L_C = k_{R4}[OH][CO] \quad [5]$$

where k_i or J_i is the reaction or photolysis rate constant for reaction i, k_d is the ozone depositional loss frequency (s^{-1}), F_{STE} is the net transport rate of ozone from the stratosphere to the troposphere (molecules cm^{-3} s^{-1}), and S_N and S_C are the source rates of NO_x and CO, respectively (molecules cm^{-3} s^{-1}). Note that the rate-limiting step for ozone production is formation of NO_2 from NO+HO_2. We further assume that the loss of NO_x (L_N) and reactive carbon (L_C) occur only through reactions R9 and R4, respectively.

To derive the dependence of OH, first we assume O_3-NO-NO_2 photochemical steady state (photostationary assumption) from reactions (R6 -R7), i.e.

$$J_{R6}\,[NO_2] = k_{R7}[NO][O_3] \quad [6]$$

We combine equation 6 with equations 1–5, and explicitly solve the linear set of equations to obtain

$$[OH] = \left(\frac{J_{R6}\,k_{R5}S_N(3[H_2O]J_{R1}k_{R2} + k_{R3}k_d[M])^{3/2}}{\sqrt{2}k_{R3}k_{R7}k_{R9}[M]^2(S_C + S_N + F_{STE})}\right) \times \sqrt{\frac{[H_2O]J_{R1}k_{R2}(2S_C - S_N + 2F_{STE}) - k_{R3}k_d[M]S_N}{k_{R8}([H_2O]J_{R1}k_{R2}(S_C + S_N - 2F_{STE}) + k_{R3}k_d[M](S_C + S_N))^2}} \quad [7]$$

Using typical tropospheric concentrations, rate constants and fluxes to identify negligible terms, eq. 7 may be reduced to a functional form of

$$[\mathrm{OH}] \propto \kappa \; J_{\mathrm{O}(^1D)}[\mathrm{H_2O}]\frac{S_N}{S_C^{3/2}} \qquad [8]$$

where $J_{\mathrm{O}(^1D)} \equiv J_{\mathrm{R1}}$ is the mass-weighted mean tropospheric photolysis frequency for ozone to $\mathrm{O}(^1D)$ (s^{-1}), $[\mathrm{H_2O}]$ is the mean tropospheric water vapor concentration (molecules cm^{-3}), S_N is the total NO_x emission rate (mol N cm^{-3} s^{-1}), and S_C is the total reduced carbon species emission rate (mol C cm^{-3} s^{-1}), and κ is an effective constant that reflects the relative weighting of the second and higher-order terms. Wang et al. (2) were the first to use a similar derivation to relate the changes in global mean [OH] to $S_N/S_C^{3/2}$, in order to describe behavior of simulated OH with and without anthropogenic emissions. Murray et al. (1) later expanded the derivation into Eq. (8) to also include the effects of climate-driven variability in water vapor and overhead ozone abundances.

S2. Adjustments to the ACCMIP archive

In multi-model inter-comparison studies, native model diagnostics must be converted into standardized fields with common units for analysis, and are therefore susceptible to definitional and unit-conversion errors. For example, *eminox* is meant to include all anthropogenic and natural NO_x sources in units of kg N m^{-2} s^{-1}; however, many models archived only anthropogenic NO_x and/or in units of kg NO m^{-2} s^{-1}. We have evaluated each archived variable against reasonable physical limits and the self-reported values in the supplemental materials of the ACCMIP overview paper (3). Assumptions made to adjust the archived values to match the requested units and variable fields or disclude fields from our analysis are outlined below.

CESM-CAM-superfast. Ozone photolysis frequencies (*photo1d*) were not archived for this model. Instead, we derive them from the production rate of OH from ozone photolysis (*prodohjo3*),

$$J_{\mathrm{O}(^1\mathrm{D})} = P(\mathrm{OH}) \cdot \frac{3.3\times10^{-11}\exp\left(\frac{55}{T}\right)[\mathrm{O_2}] + 2.15\times10^{-11}\exp\left(\frac{110}{T}\right)[\mathrm{N_2}]}{2\left(1.63\times10^{-10}\exp\left(\frac{60}{T}\right)\right)[\mathrm{H_2O}][\mathrm{O_3}]},$$

where $P(\mathrm{OH})$ is *prodohjo3* converted to molecules cm^{-3} s^{-1}, T is the local absolute temperature in K, $[\mathrm{N_2}]$, $[\mathrm{O_2}]$ and $[\mathrm{H_2O}]$ are respectively the number densities of oxygen, nitrogen and water vapor in molecules cm^{-3} determined using archived temperature, pressure and mixing ratios, and the rate constants are taken from the JPL 2011 recommendations (4).

In order to match the emissions reported by Lamarque et al. (3): we consider *eminox* to be actually archived as kg NO m^{-2} s^{-1} and without lightning NO_x or a constant 2.8 Tg N yr^{-1} of other natural sources, and for *emivoc* to be actually archived as kg isoprene m^{-2} s^{-1}.

CICERO-OsloCTM2. In order to match the emissions reported by Lamarque et al. (3), we consider all archived emissions to not include any natural sources. In this study, we add the constant natural emission fluxes reported for these simulations by Skeie et al. (5): 5 Tg N yr^{-1} of lightning NO_x and 8 Tg N yr^{-1} of other natural NO_x, 180 Tg yr^{-1} of biogenic CO, and 397 Tg C yr^{-1} of biogenic NMVOCs.

CMAM. Emissions of NMVOCs are zero in this model. The chemical loss of CO for several years of the RCP 8.5 scenario is many orders of magnitude too high, and these years are discluded from this analysis.

EMAC. In order to match the emissions reported by Lamarque et al. (3): *eminox* is considered to be actually archived as kg NO m^{-2} s^{-1}, and *emivoc* is scaled by the mass ratio of C to total mass of NMVOC assumed by the model (161/210) (6). RCP 8.5 is not included in this analysis due to non-physical archived model air masses.

GEOSCCM. All variables used in this study are correctly archived.

GFDL-AM3. Archived *eminox* did not include lightning NO_x, which we add in this analysis.

GISS-E2-R. All variables used in this study are correctly archived.

GISS-E2-TOMAS. In order to match the emissions reported by Lamarque et al. (3),*emivoc* is multiplied by the molar mass ratio of isoprene in grams (68).

HadGEM2. In order to match the emissions reported by Lamarque et al. (3), *eminox* is considered to be actually archived as kg $\mathrm{NO_2}$ m^{-2} s^{-1} and without lightning NO_x. One year of RCP 8.5 is not included in this analysis due to error in model level height precluding airmass calculation.

LMDzORINCA. Historical emissions of CO or NMVOC were not archived, so decadal mean *emico* and *emivoc* are prescribed from the values reported in Lamarque et al. (3) in this scenario.

MIROC-CHEM. In order to match the emissions reported by Lamarque et al. (3), *eminox* is considered to be actually archived as kg $\mathrm{NO_2}$ m^{-2} s^{-1} and without lightning NO_x. Lightning emissions were not archived, so decadal mean *emilnox* is prescribed from the values reported in Lamarque et al. (3).

MOCAGE. In order to match the emissions reported by Lamarque et al. (3), *eminox* is considered to be actually archived as g N m^{-2} s^{-1}, and *emico* and *emivoc* are considered to be actually archived as g C m^{-2} s^{-1}. Lightning emissions in 1983 and 2003 of the historical scenario and 2032 of the RCP 8.5 scenario are unrealistic, and not included in this analysis.

NCAR-CAM3.5. In order to match the emissions reported by Lamarque et al. (3), *eminox* is considered to be actually archived without lightning NO_x. The *emivoc* field was not archived, so decadal mean values reported by Lamarque et al. (3) are used instead. The chemical loss rates of CO (*lossco*) and methane (*lossch4*) were treated as if they were archived as molecules cm^{-3} s^{-1}, and *lossch4* was scaled by an additional factor of 0.01 for all scenarios except RCP 6.0.

STOC-HadAM3. All variables used in this study are correctly archived.

UM-CAM. All variables used in this study are correctly archived.

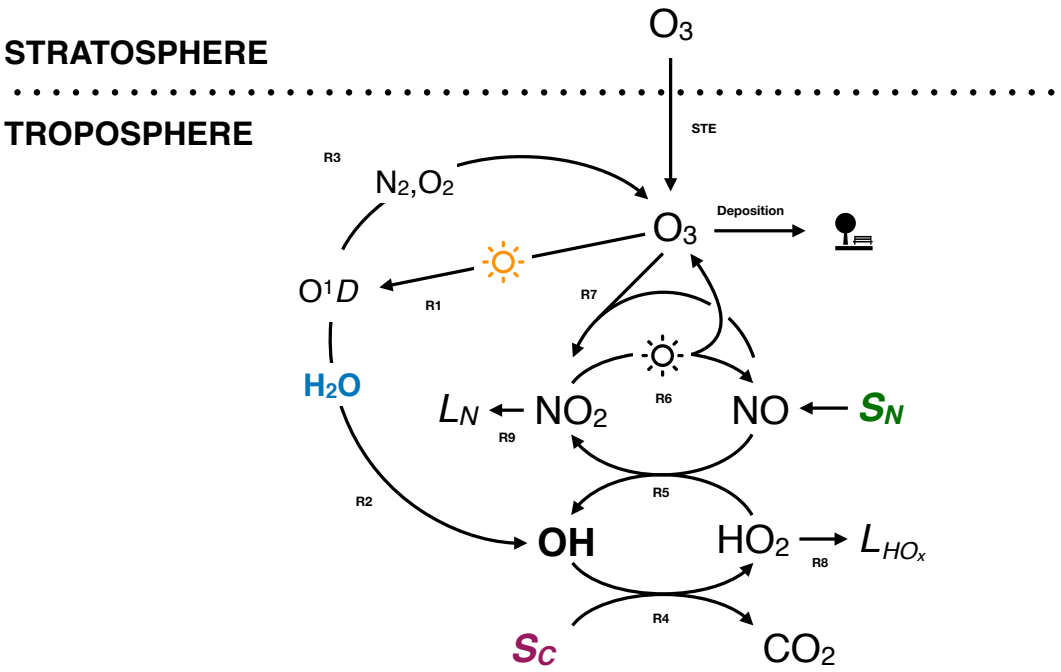

Fig. S1. Diagram of dominant chemical reactions affecting OH. The four key parameters of Eq. [1] are highlighted in colors.

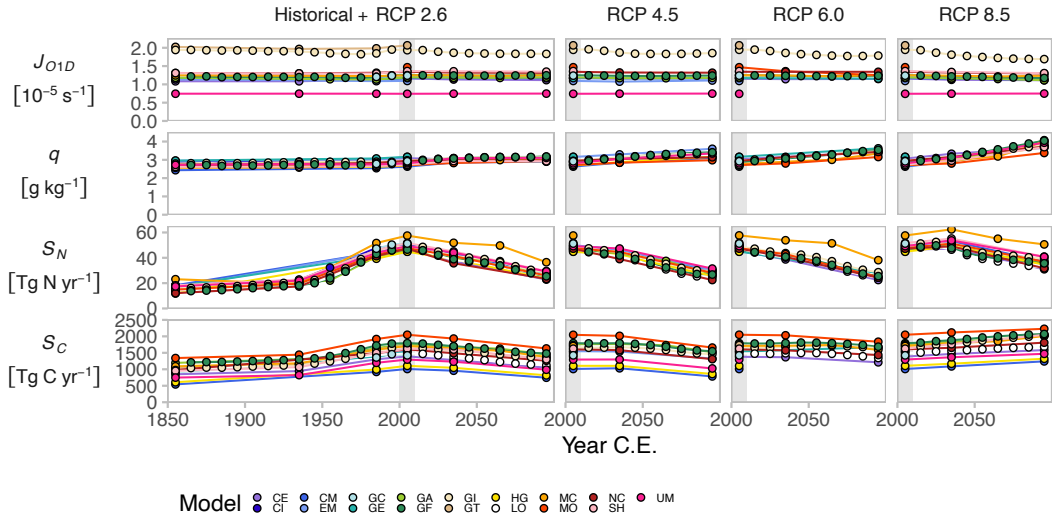

Fig. S2. Key parameters for OH photochemistry exhibit large temporal and inter-model variability in the ACCMIP simulations. *Top row:* Tropospheric mass-weighted mean decadal photolysis frequency of ozone to O(^1D) in 10^5 s^{-1}. *Second row:* Tropospheric decadal mean water vapor abundance in g H_2O per kg air. *Third row:* Decadal mean reactive nitrogen source in Tg N yr^{-1}. *Bottom row:* Decadal mean total reactive carbon source in Tg C yr^{-1}. Not all simulations submitted all variables for all experiments.

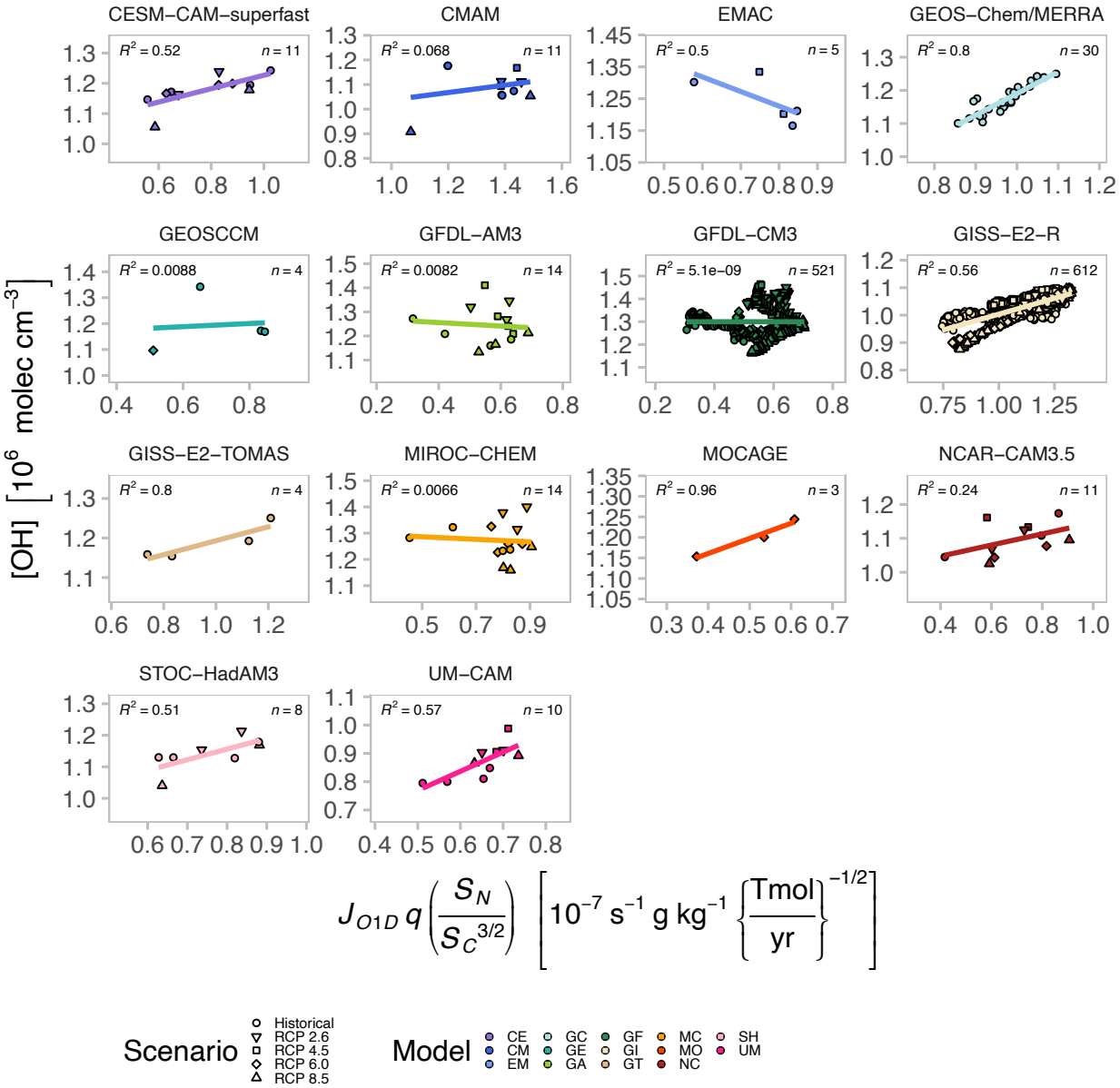

Fig. S3. Same as Fig. 2 in the main text, but with each model that contributed all four key parameters isolated, and showing annual means rather than decadal means.

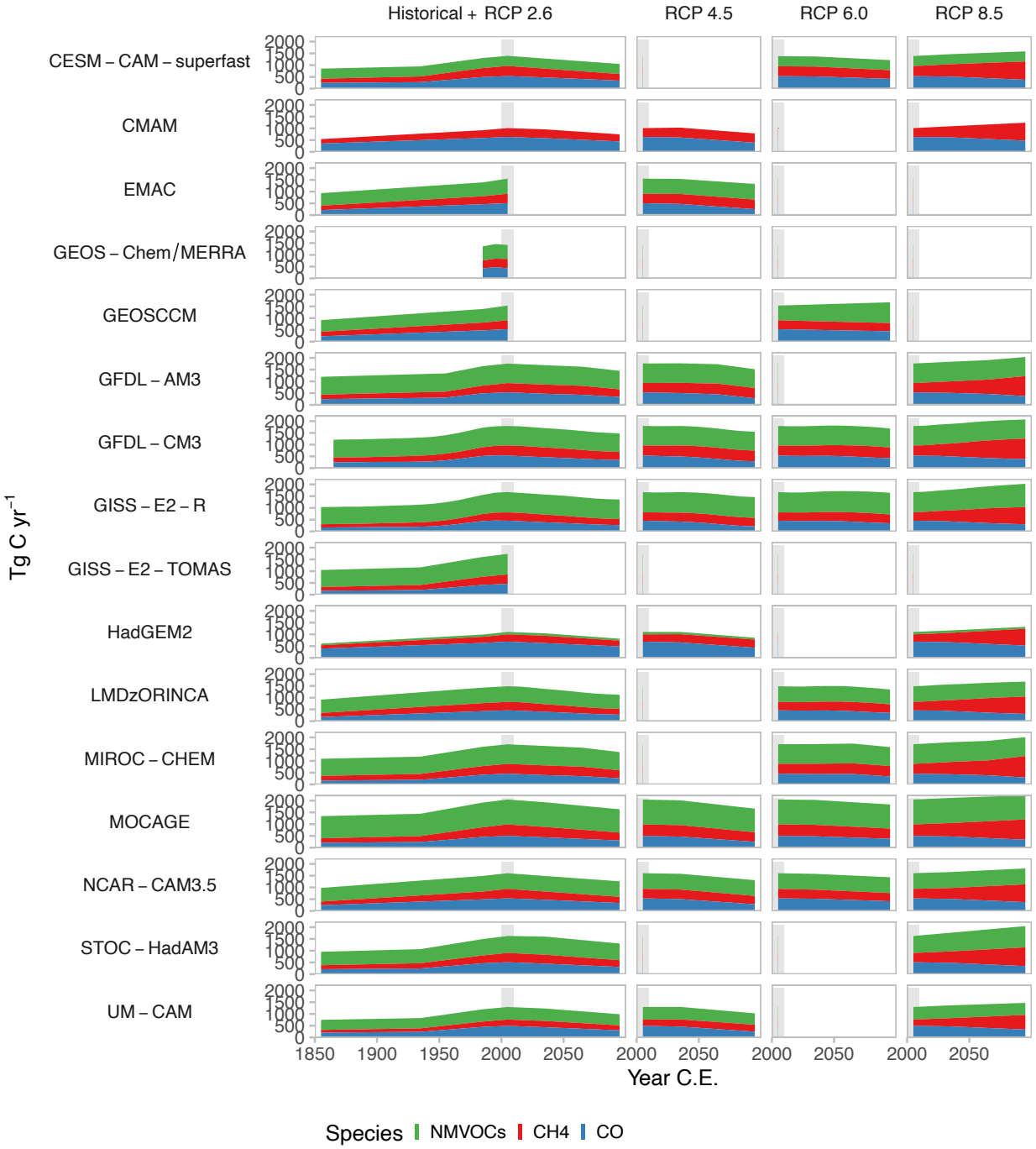

Fig. S4. Reactive carbon emission time series broken down by type. Stacked area charts indicate the magnitude of S_C associated with CO (blue), methane (red), and NMVOCs (green). Each row shows the time series for a different model.

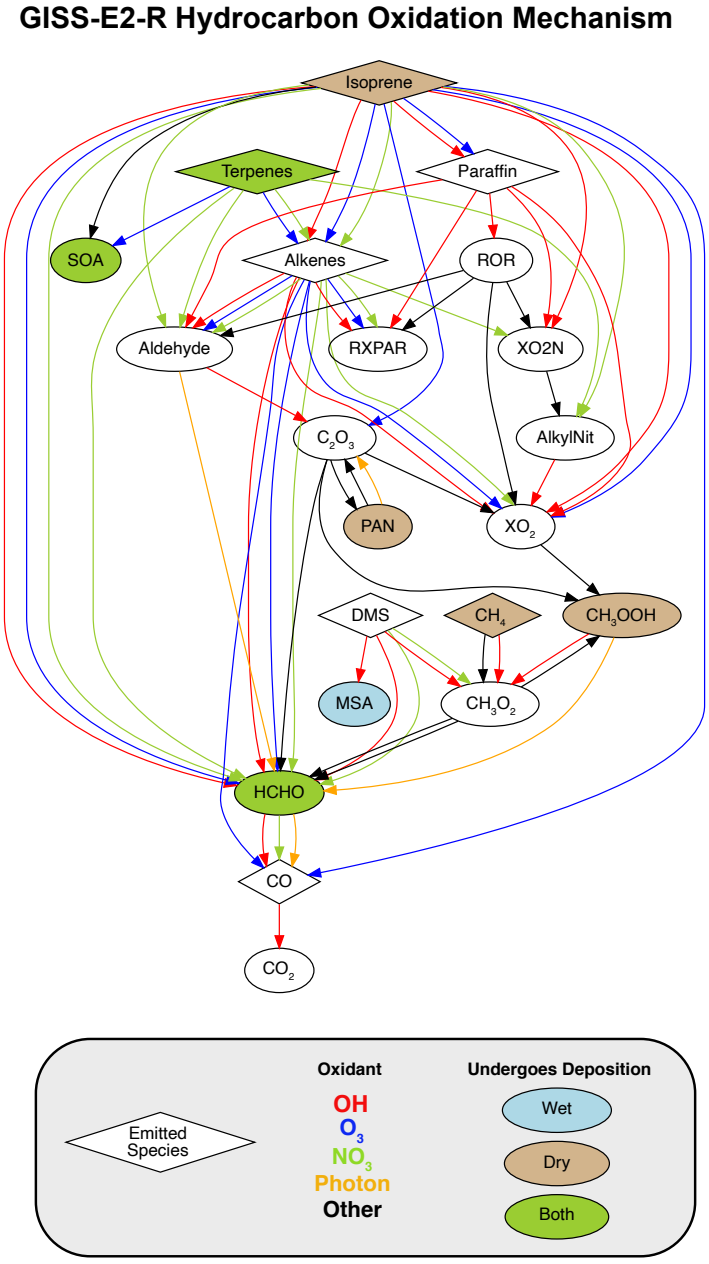

Fig. S5. Flow chart from emission to removal of reactive carbon species in the GISS-E2-R oxidation mechanism as described by Shindell et al. (7–10). Emitted reduced carbon species shown as diamonds. Chemical reactions are represented as directional arrows colored by oxidant (red = OH; blue = ozone; green = nitrate radical; orange = photolysis; black = other). Species that may be removed from the atmosphere via wet or dry deposition processes are shaded as light blue or tan, respectively. Those that may be removed by either are shaded as green.

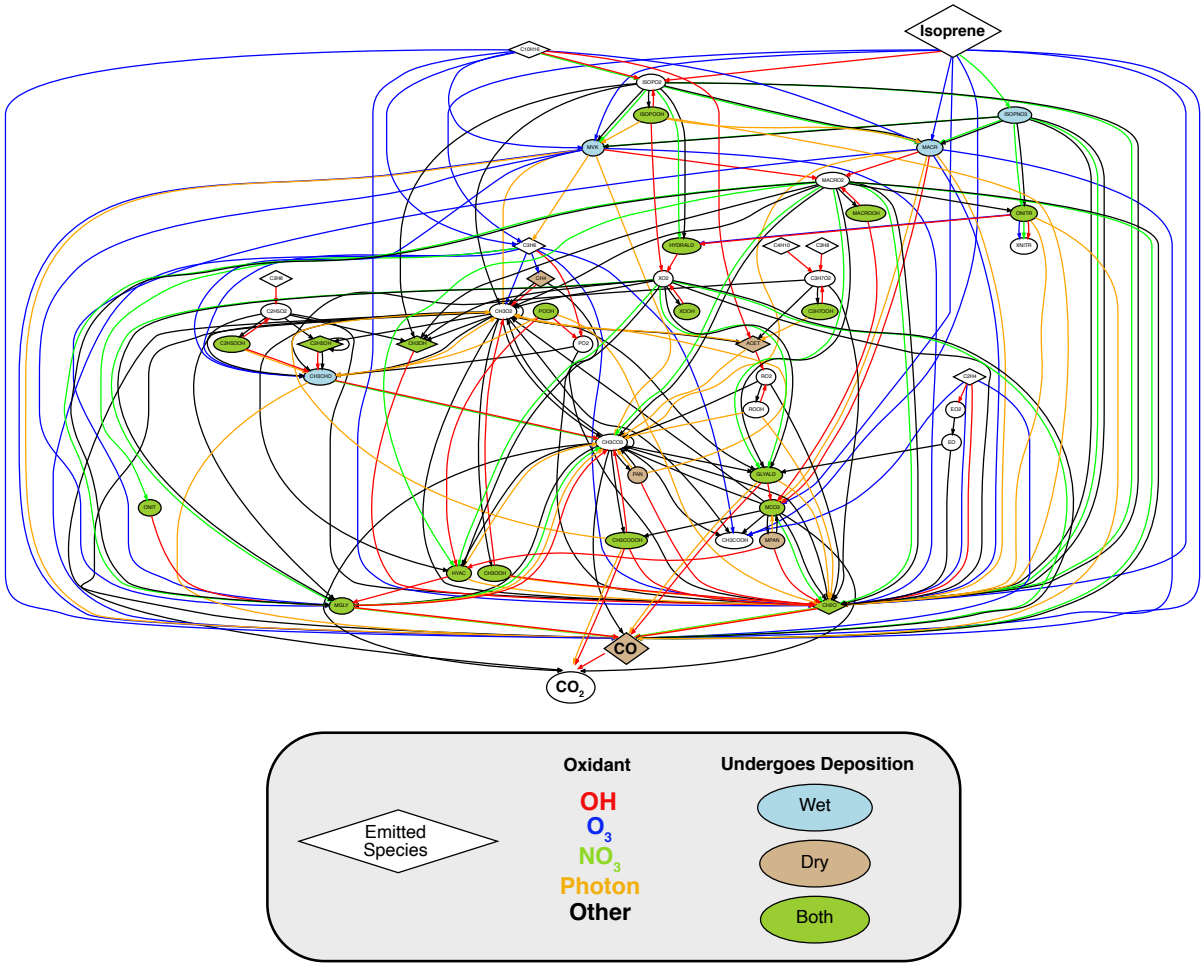

Fig. S6. Same as Fig. S5, but for the GFDL atmospheric chemical mechanism as described by Horowitz et al. (11, 12). Note, dimethylsulfide (DMS) is also emitted, but only for purposes of the global sulfur budget.

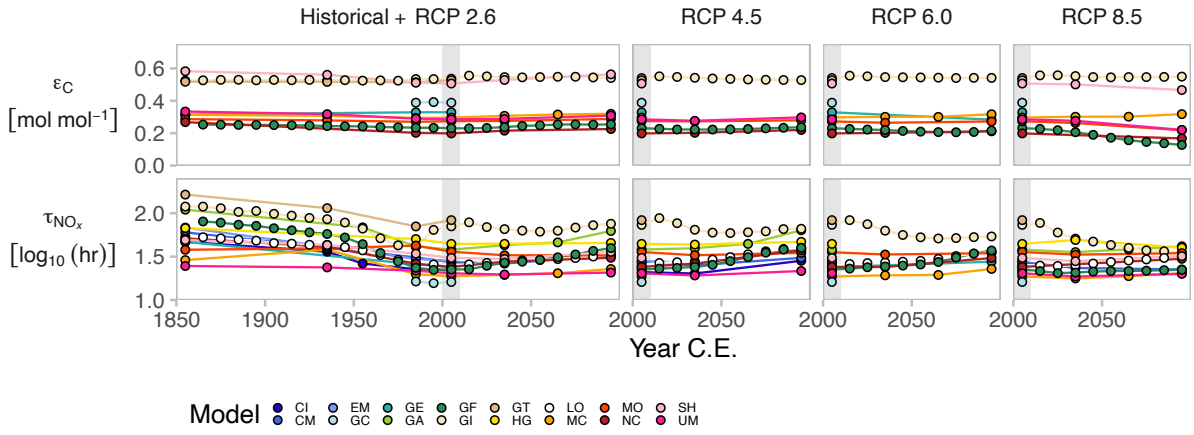

Fig. S7. Decadal mean oxidative efficiency (ϵ_{ox}; top row; unitless) and the $\log_{10}$-transformed decadal mean NO_x lifetime (τ_{NO_x}; bottom row; $\log_{10}$(hr)) in the ACCMIP simulations.

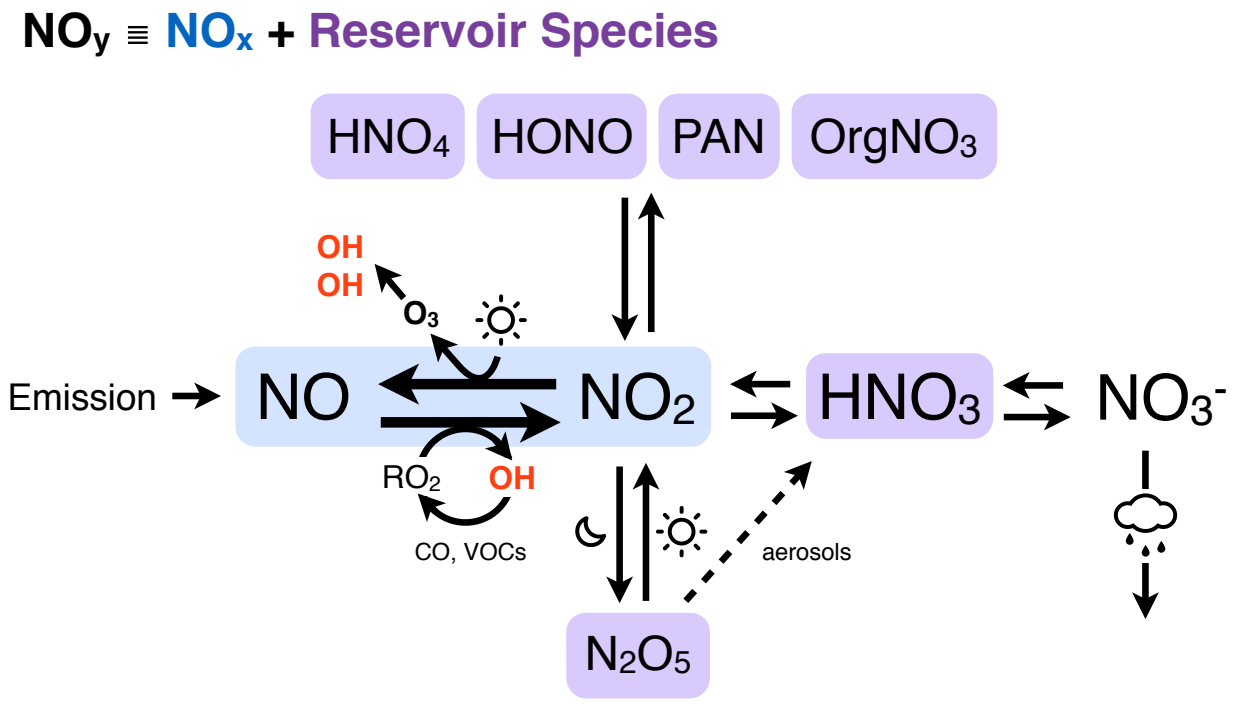

Fig. S8. Schematic of the tropospheric reactive nitrogen budget.

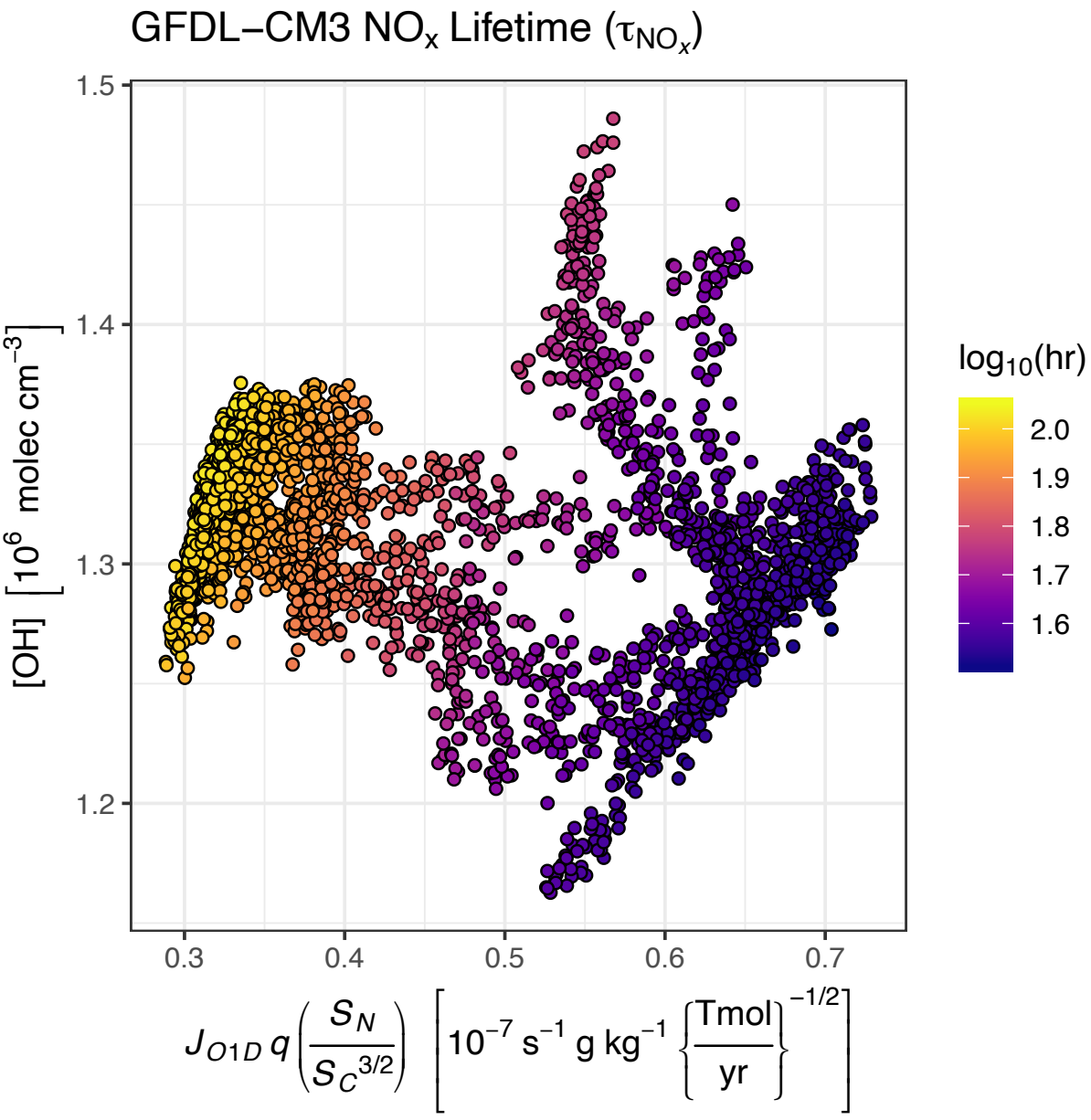

Fig. S9. Annual mean tropospheric NO_x lifetime in $\log_{10}$(hr) of the entire ensemble of GFDL-CM3 simulations contributed to CMIP5, of which the ACCMIP runs are a subset.

References

1. Murray LT, et al. (2014) Factors controlling variability in the oxidative capacity of the troposphere since the Last Glacial Maximum. *Atmos Chem Phys* 14(7):3589–3622.
2. Wang YH, Jacob DJ (1998) Anthropogenic forcing on tropospheric ozone and OH since preindustrial times. *J Geophys Res Atmos* 103(D23):31123–31135.
3. Lamarque JF, et al. (2013) The Atmospheric Chemistry and Climate Model Intercomparison Project (ACCMIP): overview and description of models, simulations and climate diagnostics. *Geosci Model Dev* 6(1):179–206.
4. Sander SP, et al. (2011) *Chemical Kinetics and Photochemical Data for Use in Atmospheric Studies*. (JPL Publication 10-6).
5. Skeie RB, et al. (2011) Anthropogenic radiative forcing time series from pre-industrial times until 2010. *Atmos Chem Phys* 11(22):11827–11857.
6. Klinger C (2011) Master's thesis (Faculty of Physics, Meteorological Institute Munich).
7. Shindell DT, Grenfell JL, Rind DH, Grewe V, Price CG (2001) Chemistry-climate interactions in the Goddard Institute for Space Studies general circulation model: 1. Tropospheric chemistry model description and evaluation. *J Geophys Res* 106(D8):8047.
8. Shindell DT, Faluvegi G, Bell N (2003) Preindustrial-to-present-day radiative forcing by tropospheric ozone from improved simulations with the GISS chemistry-climate GCM. *Atmos Chem Phys* 3(5):1675–1702.
9. Shindell DT, et al. (2006) Simulations of preindustrial, present-day, and 2100 conditions in the NASA GISS composition and climate model G-PUCCINI. *Atmos Chem Phys* 6(12):4427–4459.
10. Shindell DT, et al. (2013) Interactive ozone and methane chemistry in GISS-E2 historical and future climate simulations. *Atmos Chem Phys* 13(5):2653–2689.
11. Horowitz LW, et al. (2003) A global simulation of tropospheric ozone and related tracers: Description and evaluation of MOZART, version 2. *J Geophys Res* 108(D24):n/a–n/a.
12. Horowitz LW, et al. (2007) Observational constraints on the chemistry of isoprene nitrates over the eastern United States. *J Geophys Res* 112(D12):955.